IEEE TRANSACTIONS ON RADAR SYSTEMS

Gradient-Based Optimization of Pseudo-Random PRI Staggering

Rachel J. Chang, *IEEE Grad Student Member*, Christian C. Jones, *IEEE Grad Student Member*, Jonathan W. Owen, *IEEE Grad Student Member*, Shannon D. Blunt, *IEEE Fellow*

***Abstract*—Pulse repetition interval (PRI) staggering is known to provide expansion of unambiguous Doppler. Random PRI staggering provides further diversity since each stagger sequence can be unique, though doing so tends to incur higher Doppler sidelobes. Expanding on recent work where the Doppler response is posed as a function of the sequence of continuously-parameterized stagger values, here the formulation of a gradient-based optimization framework is shown to flatten the response over a prescribed extended Doppler interval when applied to arbitrary random stagger sequences. A metric for uniqueness between PRI sequences is also examined. Both simulated and open-air measurements demonstrate that optimization significantly improves peak sidelobe performance while maintaining uniqueness of the random instantiation (i.e. does not collapse to a single solution).**

***Index Terms*—radar signal processing, diversity methods, Doppler radar, gradient methods, radar measurements**

I. INTRODUCTION

In standard pulse-Doppler radar, pulses are transmitted with a uniform pulse repetition interval (PRI), which permits the use of simple Doppler processing via fast Fourier transform (FFT) [1-3]. However, this uniform structure also results in aliasing of the Doppler spectrum when radial motion involves a Doppler frequency shift whose magnitude exceeds one-half of the pulse repetition frequency (PRF). While mitigating such Doppler ambiguity can clearly be achieved by increasing the PRF, the reciprocal relationship of PRI = 1/PRF means the ensuing smaller PRI incurs a shortened range ambiguity.

A well-known work-around to this fixed range/Doppler ambiguity trade-space is to avoid the uniform structure by introducing variability. Arguably the more common approach, generally denoted as "PRF staggering", is to employ a fixed PRF for a coherent processing interval (CPI) that is then changed in a subsequent CPI so that ambiguities can be unwrapped via methods like the Chinese Remainder Theorem, Coincidence algorithm, or the Clustering algorithm [1,4-9].

One could alternatively impose variability within a single CPI by performing "PRI staggering" on the individual pulses (note that the PRF and PRI staggering nomenclature is sometimes used interchangeably, but here we rely on the above definitions). This manner of pulse diversity can be further categorized into either static forms in which interpulse times are taken from a finite set of values (e.g. [10,11]), structured forms for which PRIs exhibit a functional dependence on slow-time [12-15], or random forms in which PRIs are independently and randomly selected [16-25].

Random PRI staggering generally enjoys greater diversity than is realized by static or structured forms, particularly since randomness facilitates new and unique sequences on demand, though there are associated performance costs [26]. The degree of allowable random deviation from a uniform PRI structure determines how well the otherwise-repeated Doppler ambiguity mainlobes can be suppressed. Since ambiguity is conserved, higher deviation therefore tends to an average Doppler response that is flatter and approaches $1/M$, for M the number of pulses in the CPI [26]. However, greater deviation from uniform does come at the cost of range swath loss and ensuing pulse eclipsing. Moreover, individual random instantiations can still produce spurious Doppler sidelobe peaks that would likely translate into false alarms, thereby limiting the utility of purely random PRI staggering.

To address this limitation, while still realizing the diversity benefits of random PRI staggering, we propose a gradient-based approach that converts a given random instantiation into a pseudo-random PRI sequence having Doppler sidelobes that are flattened via optimization. Specifically, we leverage the parameterized stagger model developed and analyzed in [26] and apply the p-norm based gradient-descent approach developed in [27], albeit now in the context of Doppler response instead of waveform design.

Subsequent analysis of these optimized pseudo-random PRI sequences reveals that worst-case random performance (in terms of spurious peaks) can be eliminated, with corresponding design guidelines developed in the process. Moreover, with sufficient stagger design freedom the uniqueness benefit of random staggering can be preserved. Both simulated and open-air experimental measurements are used to illustrate the prospective benefits and trade-offs.

From what the authors have been able to discern, rather little attention has been paid to the optimization of random PRI staggering. In the early 1970s Prinsen [28] proposed using random initializations to optimize a cost function based on signal-to-clutter ratio in a gradient-descent manner. Then within the last year of this writing de Martin and van Rossum [29] examined the use of sparsity and genetic algorithms, which tend to produce randomized sequences. In contrast, the

This work was supported by the Office of Naval Research under Contract #N00014-20-C-1006. DISTRIBUTION STATEMENT A. Approved for public release: distribution unlimited. *(Corresponding author: Rachel J. Chang.)*

The authors are with the Radar Systems Lab (RSL) and the Electrical Engineering & Computer Science (EECS) Department, University of Kansas, Lawrence, KS 66045 USA (email: rjchang@ku.edu; c422j868@ku.edu; j842o274@ku.edu; sdblunt@ku.edu).

approach developed here relies on a stagger-parameterized version of the Doppler response from [26] that is assessed using a *p*-norm metric and optimized via gradient-descent. Of course, it is expected that a variety of other metric / optimization method combinations could conceivably arise from this framework.

II. Staggered PRI Doppler Response

It is convenient to pose the CPI of M staggered PRIs relative to a uniform CPI so a consistent dwell time is maintained for comparison (with Doppler resolution likewise fixed). Denote the mth PRI for $m = 1, 2, \ldots, M$ as the time interval

$$T_m = T_{\text{avg}} + \Delta T_m \,, \tag{1}$$

with the ΔT_m deviations independently drawn from interval $[-\delta, +\delta]$ with uniform probability and the average PRI therefore

$$T_{\text{avg}} = \frac{1}{M}\sum_{m=1}^{M} T_m \,. \tag{2}$$

Consequently, the overall CPI extent is

$$T_{\text{CPI}} = M\,T_{\text{avg}} = \sum_{m=1}^{M} T_m \,, \tag{3}$$

which we shall enforce to be a fixed value through appropriate dilation/contraction scaling since a given random (or optimized pseudo-random) instantiation of T_m values cannot be expected to satisfy a fixed total.

As developed in [26], the slow-time Doppler phase induced by a radial mover for the mth PRI can be expressed as

$$\begin{aligned} v_m(f_{\text{D}}) &= \exp\!\left(j2\pi f_{\text{D}}\, T_{\text{acc}}(m)\right) \\ &= \exp\!\left(j2\pi f_{\text{nD}}\, \varepsilon_{\text{acc}}(m)\right), \end{aligned} \tag{4}$$

where $f_{\text{D}} = 2v_{\text{rad}}/\lambda$ is Doppler frequency in Hertz for radial velocity v_{rad} and wavelength λ. The term

$$T_{\text{acc}}(m) = \sum_{q=0}^{m-1} T_q \tag{5}$$

for $m = 1, 2, \ldots, M$ in (4) is the accumulated slow-time at the start of the mth PRI, with $T_0 = \Delta T_0 = 0$, and thus $T_{\text{acc}}(1) = 0$ for the first pulse. The second line of (4) expresses slow-time phase in terms of normalized Doppler $f_{\text{nD}} = f_{\text{D}}\,T_{\text{avg}}$ and similarly normalized accumulated slow-time

$$\varepsilon_{\text{acc}}(m) = \frac{T_{\text{acc}}(m)}{T_{\text{avg}}} = \sum_{q=0}^{m-1} \varepsilon_q \,. \tag{6}$$

The summands in (6), via (1) and (5), are

$$\varepsilon_m = \frac{T_m}{T_{\text{avg}}} = 1 + \Delta\varepsilon_m \tag{7}$$

for $m = 1, 2, \ldots, M$ and with $\varepsilon_0 = \Delta\varepsilon_0 = 0$. The normalized deviations $\Delta\varepsilon_m$ in (7) thus lie on the interval

$$-\bar{\delta} \;\le\; \Delta\varepsilon_m \;\le +\bar{\delta} \quad \text{for} \quad \bar{\delta} = \delta / T_{\text{avg}}\,, \tag{8}$$

which can be expressed as a percentage. It is worth noting that the accumulation in (4)-(6) means that the staggers produce a cumulative effect that can lead to sequences that are quite different from the uniform PRI arrangement.

Using (7), now define the $M \times 1$ stagger vector

$$\begin{aligned} \boldsymbol{\varepsilon} &= [\varepsilon_0 \;\; \varepsilon_1 \;\; \varepsilon_2 \cdots \; \varepsilon_{M-1}]^T \\ &= [0 \;\; \mathbf{1}_{(M-1)\times 1}^T]^T + [0 \;\; \Delta\varepsilon_1 \;\; \Delta\varepsilon_2 \cdots \; \Delta\varepsilon_{M-1}]^T, \end{aligned} \tag{9}$$

where $\mathbf{1}_{(M-1)\times 1}$ is a vector of ones and the bottom line of (9) collects the set of $M-1$ optimizable parameters (i.e. the $\Delta\varepsilon_m$ terms). Also define the $M \times M$ lower triangular matrix $\mathbf{B}$ that has ones on/below the main diagonal and zeros above. Consequently, we can express (6) via (9) as

$$\varepsilon_{\text{acc}}(m) = \mathbf{b}_m^T \boldsymbol{\varepsilon} \tag{10}$$

with $\mathbf{b}_m$ containing the elements from the mth row of $\mathbf{B}$, i.e.

$$[\mathbf{b}_1 \;\; \mathbf{b}_2 \cdots \mathbf{b}_M] = \mathbf{B}^T, \tag{11}$$

for $(\bullet)^T$ the transpose operation. Thus, (4) becomes

$$v_m(f_{\text{nD}}) = \exp\!\left(j2\pi f_{\text{nD}}\, \mathbf{b}_m^T \boldsymbol{\varepsilon}\right), \tag{12}$$

noting the change to dependence on normalized Doppler f_{nD}. By extension, the $M \times 1$ stagger-parameterized Doppler steering vector becomes

$$\begin{aligned} \mathbf{v}(f_{\text{nD}}) &= \left[1 \;\; \exp(j2\pi f_{\text{nD}}\, \varepsilon_{\text{acc}}(2)) \cdots \; \exp(j2\pi f_{\text{nD}}\, \varepsilon_{\text{acc}}(M))\right]^T \\ &= \exp\{j2\pi f_{\text{nD}}\, \mathbf{B}\,\boldsymbol{\varepsilon}\}, \end{aligned} \tag{13}$$

with $\exp\{\bullet\}$ denoting element-wise exponentiation. Note that if $\Delta\varepsilon_1 = \Delta\varepsilon_2 = \cdots = \Delta\varepsilon_{M-1} = 0$, then (13) reverts to the usual Vandermonde form for uniform PRI.

Subsuming beamforming, pulse compression, and in-phase/quadrature (I/Q) sampling it is shown in [26][1] that the received signal model for Doppler processing can be written as

[1] For simplicity, we are excluding the tilde notation on the scattering and noise terms from where (14) was derived in [26] since the same level of modeling detail is not required here.

$$\mathbf{z}(\ell) = \sum_{f_{\mathrm{nD}}} x(\ell; f_{\mathrm{nD}})\, \mathbf{v}(f_{\mathrm{nD}}) + \mathbf{n}(\ell) \approx \mathbf{V}\mathbf{x}(\ell) + \mathbf{n}(\ell)\,, \tag{14}$$

where $x(\ell; f_{\mathrm{nD}})$ is the scattering in the ℓth range bin corresponding to Doppler steering vector $\mathbf{v}(f_{\mathrm{nD}})$, and $\mathbf{n}(\ell)$ is an $M \times 1$ vector of additive noise. Discretizing the Doppler continuum then yields the approximation in the bottom line of (14), with the columns of matrix $\mathbf{V}$ the Doppler steering vectors associated with individual scattering elements in $\mathbf{x}(\ell)$.

Nominal discretization of Doppler given uniform PRI would involve M equally-spaced Doppler frequencies on the interval $f_{\mathrm{D}} \in [-\mathrm{PRF}/2, +\mathrm{PRF}/2]$ (or $f_{\mathrm{nD}} \in [-1/2, +1/2]$ in normalized form), with finer granularity realized via oversampling by factor K. Sufficient PRI staggering provides an extension of the Doppler interval above by factor $\beta \geq 1$, yielding $N = \lceil \beta K M \rceil$ total steering vectors for ceiling operation $\lceil \bullet \rceil$. Thus, matrix $\mathbf{V}$ is $M \times N$ and can be written as

$$\mathbf{V} = \exp\left\{ j 2\pi\, \mathbf{B}\, \boldsymbol{\varepsilon}\, \mathbf{f}_{\mathrm{nD}}^{T} \right\}, \tag{15}$$

again using element-wise exponentiation and with vector $\mathbf{f}_{\mathrm{nD}}$ containing N normalized frequency values after discretization. If N is even-valued, it is useful to insert an additional term so that zero Doppler is included.

The value of β arises from the *least common multiple* over the set of $(1/T_m)$ values, which could include Doppler frequencies that far exceed physical reality (especially if irrational values are permitted). In [26] it was suggested that a reasonable β_{mov} value be used instead that sufficiently captures the radial velocities (and ensuing Doppler frequencies) of realistic movers.

Here, since we are seeking to optimize a sequence of stagger values that provide a sufficiently flattened response over the expanded interval $f_{\mathrm{nD}} \in [-\beta_{\mathrm{mov}}/2, +\beta_{\mathrm{mov}}/2]$, it is useful to introduce the term β_{opt} for the intended optimization interval. Because the scattering from a large mover at one edge of this interval would induce a Doppler sidelobe response at the opposite edge, it is therefore appropriate to set $\beta_{\mathrm{opt}} = 2\beta_{\mathrm{mov}}$. Moreover, since it may be necessary to dilate/contract some random (or optimized pseudo-random) set of T_m values to achieve a prescribed (and fixed) T_{CPI}, it is useful to increase β_{opt} a modest amount further (see Section III-C).

The relative Doppler response between two frequencies is shift-invariant, meaning that consideration of the zero-referenced response yields a general performance assessment for the entire Doppler span of interest. Therefore, denote $\mathbf{v}_0 = \mathbf{1}_{M\times 1}$ for $f_{\mathrm{nD}} = 0$ so that the zero-referenced Doppler response is $u(f_{\mathrm{nD}}) = \mathbf{v}^H(f_{\mathrm{nD}})\, \mathbf{v}_0$, which translates into the $N \times 1$ gain-normalized, discretized vector

$$\mathbf{u}(\boldsymbol{\varepsilon}) = \frac{1}{M} \mathbf{V}^H \mathbf{v}_0 \tag{16}$$

for $(\bullet)^H$ the Hermitian operation. Here, we have explicitly denoted dependence on the $M \times 1$ stagger vector $\boldsymbol{\varepsilon}$ from (9). The parameters in $\boldsymbol{\varepsilon}$ lie on a (bounded) continuum and thus each element of (16) is a continuous function of these parameters, thereby permitting determination of a gradient.

It was shown in [26] that the closed-form solution

$$E\left[\left| \frac{1}{M} \mathbf{v}^H(f_{\mathrm{nD}}) \mathbf{v}_0 \right|^2 \right] = \frac{1}{M} + \frac{2}{M^2} \sum_{m=1}^{M-1} \left(m \cos\left(2\pi f_{\mathrm{nD}} (M-m)\right) \times \left[\mathrm{sinc}(2\pi f_{\mathrm{nD}} \bar{\delta}) \right]^{(M-m)} \right) \tag{17}$$

is obtained by taking the expectation of the magnitude-square of the zero-referenced Doppler response as a function of the number of pulses M and normalized stagger limit $\bar{\delta} = \delta / T_{\mathrm{avg}}$. Fig. 1 plots (17) for different values of $\bar{\delta}$ and for M = 100, where it is observed that increasing the stagger limit yields a progressively flatter expectation response that is tending toward $-10 \log_{10}(M = 100) = -20$ dB.

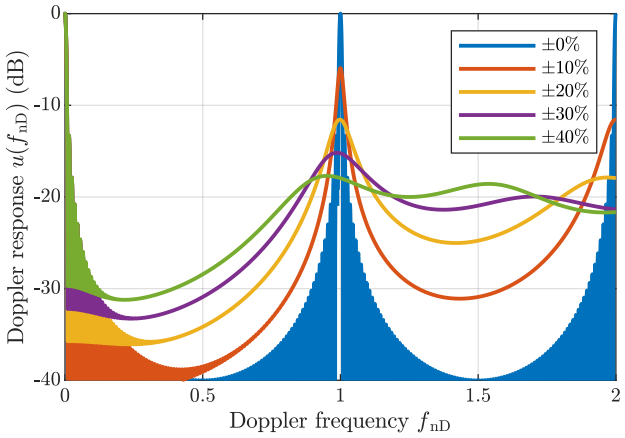

Fig. 1. Expectation of zero-referenced Doppler response per (17) for different limits on random staggering and M = 100 pulses

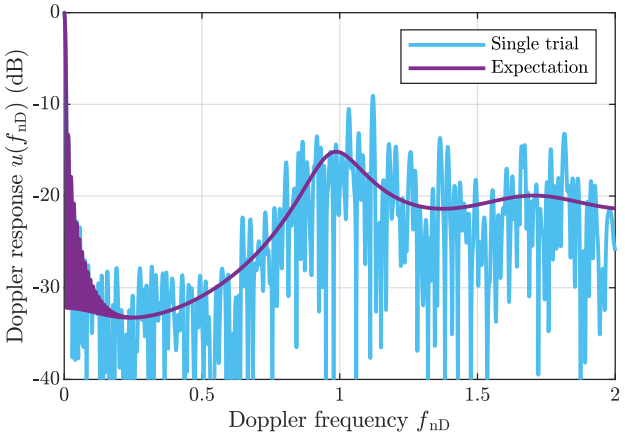

Fig. 2. Single instantiation of random staggering for ±30% limits compared to expectation via (17), illustrating Doppler sidelobe variation

While Fig. 1 suggests flatter Doppler sidelobes are achieved with sufficient random staggering, the expected response does not tell the whole story since it only represents the mean. In contrast, consider the single random instantiation in Fig. 2 for

30% staggering. While we do see a general flattening relative to a uniform PRI (the 0% case in Fig. 1), we also observe some undesirable random sidelobe peaks that would likely translate into false alarms in a subsequent detection stage of the radar. Consequently, there remains a need to optimize the set of staggers into a pseudo-random form to ensure a flatter response in each instantiation (i.e. reduce the variance). Note that, as demonstrated in [26], there is essentially a conservation of mainlobe/sidelobe energy in each Doppler ambiguity interval so that a flattened response approaching $-10\log_{10}(M)$ is the best that one can achieve.

III. Staggered PRI Gradient-Descent Optimization

The following develops a cost function that is appropriate for the particular problem of staggered PRI optimization in which the desired goal is to flatten Doppler sidelobes out to some multiple β_{opt} of the nominal [–PRF/2, +PRF/2] interval. Because this cost function is posed as a continuous function of the underlying stagger parameters, the gradient is then determined for use in a gradient-descent framework.

A. PRI Staggering Cost Function

The random PRI formulation discussed above and analytically evaluated in [26] is based on bounded deviations from the uniform PRI structure. While preservation of the $[-\overline{\delta},+\overline{\delta}]$ normalized limits could be achieved by introducing constraints into the optimization framework, we instead rely on a bounding function imposed as

$$\varepsilon_m = 1+\Delta\varepsilon_m \triangleq 1+\overline{\delta}\sin(\alpha_m) \tag{18}$$

for m = 1, 2, …, $M-1$ (recall that $\varepsilon_0 = 0$) such that (8) is satisfied with any real-valued α_m. Collecting these terms into the $M\times 1$ vector $\boldsymbol{\alpha} = [0\ \alpha_1\ \alpha_2 \cdots \alpha_{M-1}]^T$ leads to the continuous functional dependence $\boldsymbol{\varepsilon}(\boldsymbol{\alpha}) \to \mathbf{u}(\boldsymbol{\alpha})$ per (16), meaning the ability to compute a gradient is likewise preserved.

Since the goal is to flatten the sidelobes within some prescribed Doppler interval, a p-norm cost function is a judicious choice. Specifically, we make use of the generalized integrated sidelobe level (GISL) metric that was employed in [27,30] for radar waveform optimization, which in the PRI staggering context takes the form

$$J_p(\boldsymbol{\alpha}) = \frac{\left\|\mathbf{w}_{\text{sl}} \odot \mathbf{u}(\boldsymbol{\alpha})\right\|_p^2}{\left\|\mathbf{w}_{\text{ml}} \odot \mathbf{u}(\boldsymbol{\alpha})\right\|_p^2} \tag{19}$$

for $2 \le p < \infty$ and with $\odot$ the Hadamard product. When p = 2, (19) becomes an integrated Doppler sidelobe level (IDSL) metric, while letting $p \to \infty$ likewise realizes a peak Doppler sidelobe level (PDSL) metric. The latter is more useful to yield a flatter response since it seeks to minimize the largest sidelobe (i.e. a *minimax* approach), though numerical instability can arise if p is too large. It was shown in [27] in the waveform design context that modest values of p can suffice; thus we shall limit attention to p = 10 here as well without loss of generality.

The $N\times 1$ selection vectors $\mathbf{w}_{\text{ml}}$ and $\mathbf{w}_{\text{sl}}$ are comprised of ones and zeros to extract the respective mainlobe and sidelobe regions of $\mathbf{u}(\boldsymbol{\alpha})$, with the latter subsuming the extended Doppler region available due to staggering out to the limit specified by β_{opt}. The vector $\mathbf{w}_{\text{ml}}$ selects for the nominal mainlobe, which corresponds to $f_{\text{nD}} \in [0, 1/M]$, noting Dopper response symmetry.

For $\mathbf{w}_{\text{sl}}$ the obvious choice would be to select for $f_{\text{nD}} \in [1/M, 0.5\beta_{\text{opt}}]$. However, as Figs. 1 and 2 illustrate, the nominal sidelobe interval within $f_{\text{nD}} \in [1/M, 0.5]$ is not greatly affected by staggering, which can be understood based on the notion of Doppler "slope deflection" discussed in [26]. Moreover, the closest sidelobe to the mainlobe could readily dominate the GISL metric, despite the fact that staggering has almost no impact upon it. Consequently, to prevent the optimization from becoming fixated on this nominal Doppler interval, we instead define $\mathbf{w}_{\text{sl}}$ to select $f_{\text{nD}} \in [0.5, 0.5\beta_{\text{opt}}]$. Put another way, the interval $f_{\text{nD}} \in [1/M, 0.5]$ is being ignored.

Finally, it is worth noting that (19) is a nonconvex function of $\boldsymbol{\alpha}$, even ignoring the cyclic structure imbued by the sinusoidal mapping into $\boldsymbol{\varepsilon}$. Consequently, there will exist many local minima solutions that may realize qualitatively similar performance in terms of flattened Doppler sidelobes. Since the particular local minima attained depends on the given random initialization, we can therefore reasonably assume that each optimized pseudo-random stagger sequence obtained is unique, with a metric to that effect proposed and evaluated in Section IV-C.

B. Gradient-Descent Optimization

In [27] the gradient was determined for the GISL cost function within the context of frequency modulated (FM) waveforms parameterized according to the polyphase-coded FM (PCFM) signal structure [31,32], leading to physically realizable signals that were demonstrated experimentally in hardware. This approach was also recently extended to other "quasi-bases" for FM waveform optimization [33]. Here we leverage portions of that derivation since the GISL cost function is likewise employed, though the underlying Doppler signal model developed above does involve a distinctly different functional relationship.

As derived in Appendix A, the gradient of (19) with respect to the $\boldsymbol{\alpha}$ parameters takes the form

$$\nabla_{\boldsymbol{\alpha}} J_p = \frac{4\pi\overline{\delta}}{M} J_p\, \mathbf{G}^T \left[\frac{\mathbf{w}_{\text{sl}}}{\mathbf{w}_{\text{sl}}^T|\mathbf{u}|^p} - \frac{\mathbf{w}_{\text{ml}}}{\mathbf{w}_{\text{ml}}^T|\mathbf{u}|^p} \right], \tag{20}$$

where the $N\times 1$ columns of matrix $\mathbf{G} = [\mathbf{0}_{N\times 1}\ \ \mathbf{g}_1 \cdots \mathbf{g}_{M-1}]$ are

$$\mathbf{g}_m = |\mathbf{u}|^{(p-2)} \odot \Im\left\{ \left(\left(\mathbf{V}^H \odot \left(\mathbf{f}_{\text{nD}} (\cos\{\boldsymbol{\alpha}\} \odot \mathbf{e}_m)^T \mathbf{B}^T \right) \right) \mathbf{v}_0 \right) \odot \mathbf{u}^* \right\} \tag{21}$$

via (39) and (37), respectively. Here, $\Im\{\bullet\}$ extracts the imaginary part of the argument, $\mathbf{e}_m$ is an $M\times 1$ elementary vector with a 1 in the mth element and zero otherwise, and $(\bullet)^*$ denotes complex conjugation. In Section IV we examine a particular implementation of this gradient to assess the

achievable performance enhancement and other behavioral attributes.

C. Contraction / Dilation Scaling to Preserve CPI Extent

A random or pseudo-random (after optimization) stagger sequence must be scaled to preserve a fixed T_{CPI}, though the pulse length remains unchanged. Accounting for the final (Mth) PRI as well, consider two extreme cases of CPI contraction/dilation in which $M-1$ PRIs exhibit all maximum (or all minimum) staggers of $\varepsilon_m = 1 \pm \bar{\delta}$ and the single remaining PRI (denoted $\tilde{m}$) conversely has the minimum/maximum of $\varepsilon_{\tilde{m}} = 1 \mp \bar{\delta}$. Noting via (3) that the intended normalized CPI extent is $T_{\text{CPI}}/T_{\text{avg}} = M$, the required scaling factor using (6) and (7) is therefore

$$\frac{M}{\left((M-1)(1\pm\bar{\delta})+(1\mp\bar{\delta})\right)} = \frac{M}{\left(M\pm(M-1)\bar{\delta}\mp\bar{\delta}\right)} \approx \frac{1}{(1\pm\bar{\delta})}. \quad (22)$$

Assuming M is sufficiently large produces the approximation in (22). Thus, the final normalized and scaled extent for the $\tilde{m}$th PRI is

$$\varepsilon_{\tilde{m},\text{scale}} \approx (1\mp\bar{\delta})/(1\pm\bar{\delta}), \quad (23)$$

which can be viewed as a bound on the largest/smallest PRI that could be obtained.

Since the bounds in (23) violate the per-PRI stagger limits of $1\pm\bar{\delta}$ when performing scaling for the CPI extent, the degree to which random/optimized staggering instantiations actually approach these bounds merits examination. Fig. 3 depicts the results from 1000 independent Monte Carlo trials as a function of $\bar{\delta}$, illustrating the longest/shortest PRI after scaling (short dashed traces) determined over the entire set of trials. The individual PRI limits of $1\pm\bar{\delta}$ (long dashed traces) and the bounds above (solid traces) are included for comparison. In short, we observe that even the worst cases in 1000 trials exceed the $1\pm\bar{\delta}$ per-PRI limits by only a small amount.

The histogram in Fig. 4 further illustrates this effect via the distribution of 10^5 randomly staggered PRIs after scaling (for sets of $M = 100$), with the dashed trace denoting the uniform distribution used for stagger generation based on $\bar{\delta} = 30\%$. A small tail is observed on each side, indicating the design boundary on minimum and maximum PRI is slightly violated due to scaling, though the degree and amount are rather small. The right side of the histogram, indicative of the case when large PRIs are dilated, exhibits a slightly longer tail than the left side, when small PRIs are contracted. This behavior agrees with Fig. 3, where dilation posed a higher tendency to exceed the design boundary.

Of the two extremes, contraction could be problematic from the perspective of loss in the shortest PRI interval (i.e. exacerbating blind ranges), yet the worst case we observe is nearly identical to the $1-\bar{\delta}$ lower PRI limit. Conversely, the dilation case impacts the Doppler span (which contracts), with Fig. 3 suggesting that an expansion of β_{opt} by the factor $1+\bar{\delta}$ should be sufficient to accommodate the instances where scaling otherwise pulls an unoptimized portion of Doppler into the span of interest. Of course, one could also choose to dicard any random instantiation having PRIs that are too large or small, though doing so would mean the computational cost of optimization is essentially wasted.

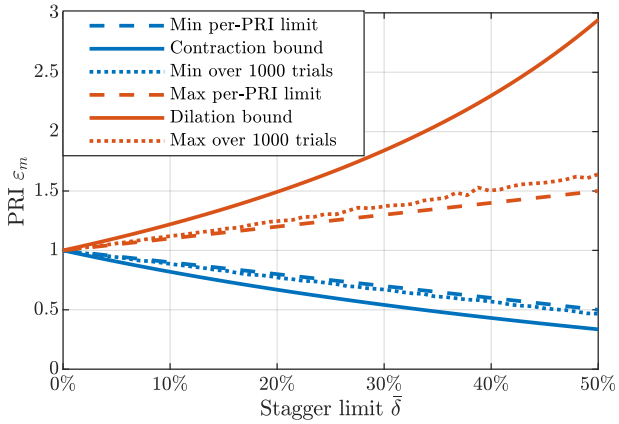

Fig. 3. Minimum/maximum PRIs (after scaling) for 1000 trials of M = 100 pulses as a function of $\bar{\delta}$ along with per-PRI limits and scaling bounds (23)

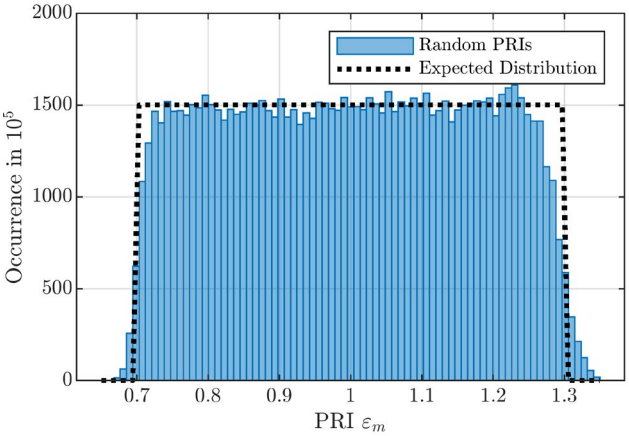

Fig. 4. Histogram of randomly generated and scaled PRIs for 1000 trials of M = 100 pulses and $\bar{\delta} = 30\%$

IV. Assessment of Staggering Optimization

Given (20) and (21), there are many gradient-based optimization methods that one could employ. Here we use the limited-memory Broyden–Fletcher–Goldfarb–Shanno (BFGS) algorithm [34], which is an unconstrained quasi-Newton method that only requires a gradient calculation each iteration (i.e. avoids determining the Hessian). In the results that follow, the particular implementation involves using the "minf_lbfgs" function in Tensorlab [35], with the objective function's iterative difference tolerance set to 10^{-7} and the step-size tolerance set to 10^{-8}.

Independent random draws from a uniform distribution on $[-\pi, +\pi]$ are used to initialize the $M-1$ values of α_m, which along with $\bar{\delta}$ produce an initial random stagger sequence via (18). Because the Doppler response is symmetric about zero, only the $f_{\text{nD}} \in [0, 0.5\beta_{\text{opt}}]$ frequency interval is shown.

A. PRI Staggering Optimization Examples

Figs. 5 and 6 illustrate two particularly severe examples of

high PDSL (formally defined in Section IV-B) resulting from random stagger instantiations. Indeed, these were the worst cases observed over 1000 independent trials for $M = 100$ pulses and $\bar{\delta} = 30\%$. Gradient-based optimization respectively achieves 9.8 dB and 8.8 dB reduction in PDSL for these cases when β_{opt} is set to 4 (along with a $1+\bar{\delta}$ extension to account for possible Doppler span contraction). Most notably, the optimization serves to eliminate the spurious peaks that would otherwise likely translate into false alarms.

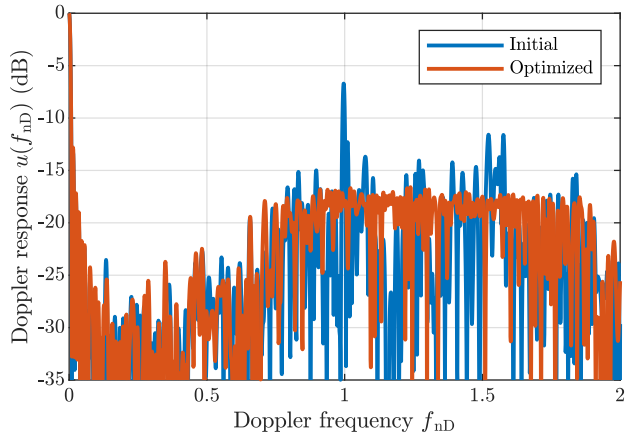

Fig. 5. Single instantiation of random staggering for $M = 100$ and $\bar{\delta} = 30\%$ compared to gradient-based optimization (9.8 dB PDSL improvement)

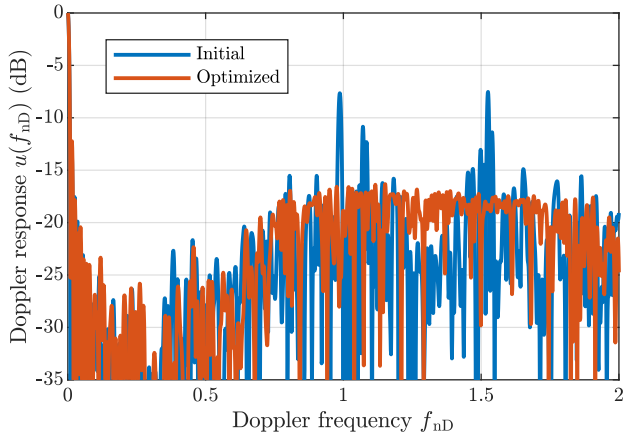

Fig. 6. Single instantiation of random staggering for $M = 100$ and $\bar{\delta} = 30\%$ compared to gradient-based optimization (8.8 dB PDSL improvement)

We again observe that the nominal Doppler interval $f_{\text{nD}} \in [0, 0.5]$) essentially follows the roll-off one expects from a uniform PRI, with modest deviation for $f_{\text{nD}} \in [0.25, 0.5]$ that is nonetheless still well below the level of the extended Doppler span. As noted in Section III-A, this behavior can be explained by the notion of phase "slope deflection" discussed in [26], where a sufficient amount of Doppler offset is necessary before any meaningful deviation from the standard uniform-PRI Doppler response is actually observable.

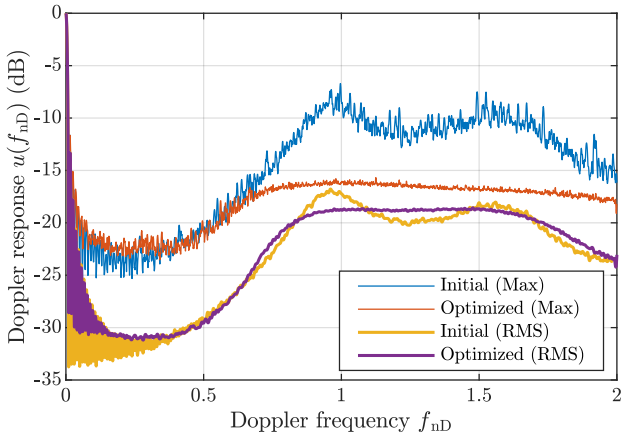

Fig. 7. Aggregate mean and maximum of random staggering for $M = 100$ and $\bar{\delta} = 30\%$ compared to gradient-based optimization

Fig. 7 then illustrates the advantage of optimization when the Doppler response is examined in aggregate across the entire set of 1000 independent staggering trials. Specifically, while the root-mean-square (RMS) responses are quite similar for the initial and optimized versions, albeit with a modest flattening of the latter, the maximum response at each f_{nD} value across the 1000 trials reveals a 2-10 dB difference. Interestingly, the most significant difference for the maximum response occurs at/near $f_{\text{nD}} = 1$, which corresponds to spurious peak locations in the examples of Figs. 5 and 6 and aligns with the first ambiguity for 0% staggering in Fig. 1. This consistent behavior suggests that some random instantiations retain a degree of uniform PRI structure. Moreover, we observe that the RMS (purple) and maximum (red) responses after optimization are now much closer, indicating significant variance reduction. In short, optimization avoids the worst-case conditions that randomness may induce.

B. Numerical Analysis of PRI Staggering Optimization

Let us now formally state a couple useful metrics for analysis. The $p = 2$ version of (19), normalized by the optimization interval β_{opt}, realizes the integrated Doppler sidelobe (IDSL)[2] metric

$$\text{IDSL} \triangleq \frac{\left\|\mathbf{w}_{\text{sl}} \odot \mathbf{u}\right\|_{p=2}^2}{\beta_{\text{opt}} \left\|\mathbf{w}_{\text{ml}} \odot \mathbf{u}\right\|_{p=2}^2}, \tag{24}$$

for $\mathbf{w}_{\text{sl}}$ encompassing the extended interval $f_{\text{nD}} \in [0.5, 0.5\beta_{\text{opt}}]$, and $\mathbf{w}_{\text{ml}}$ selecting the mainlobe $f_{\text{nD}} \in [0, 1/M]$. Similarly, the peak Doppler sidelobe level (PDSL) metric can be expressed as

$$\text{PDSL} \triangleq \frac{\left\|\mathbf{w}_{\text{sl}} \odot \mathbf{u}\right\|_{p\to\infty}^2}{\left\|\mathbf{w}_{\text{ml}} \odot \mathbf{u}\right\|_{p\to\infty}^2} = \frac{\max\limits_{f_{\text{nD}}} \left|\mathbf{w}_{\text{sl}} \odot \mathbf{u}\right|^2}{\max\limits_{f_{\text{nD}}} \left|\mathbf{w}_{\text{ml}} \odot \mathbf{u}\right|^2}, \tag{25}$$

[2] In [26] IDSL was defined to comprise only the nominal normalized Doppler interval $f_{\text{nD}} \in [0, 0.5]$ while an extended version thereof denoted as EDSL expanded to include $f_{\text{nD}} \in [0, 0.5\beta]$ for arbitrary β to illustrate the distinction between interval extent. Here we only consider the extended interval so simply use the moniker IDSL as a catch-all since it is directly analogous to integrated sidelobe level (ISL) in waveform optimization.

which simply computes the ratio of the largest Doppler sidelobe (over the extended interval) to the mainlobe value at $f_{nD} = 0$.

We can then apply these metrics to the previous two sets (initial and optimized) of 1000 random PRI stagger sequences that have $M = 100$ pulses, ±30% limits and $\beta_{opt} = 4$. First consider the IDSL metric of (24), with Fig. 8 depicting the ensuing histogram for each set of stagger sequences. From this perspective the benefit of optimization is underwhelming, with significant overlap between the histograms and optimization providing only about 0.1 dB improvement when viewed in totality. Of course, like its waveform optimization counterpart ISL, the IDSL metric captures a collective sidelobe response, and per Fig. 7, the RMS initial and optimized results are similar.

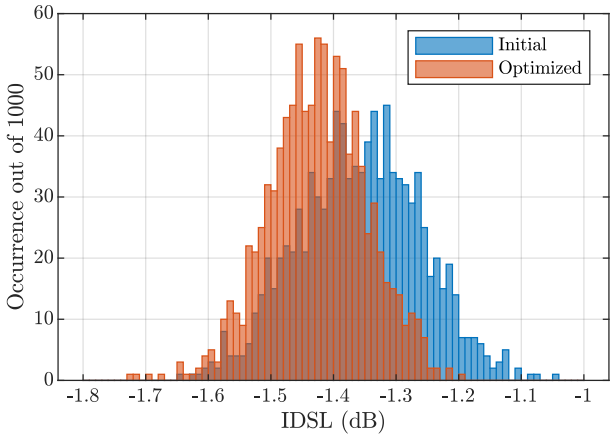

Fig. 8. Histogram of IDSL from (24) for 1000 independent initial and optimized random stagger sequences for $M = 100$, $\bar{\delta} = 30\%$, and $\beta_{opt} = 4$

In contrast, since the purpose of optimization here is to flatten staggered Doppler responses so that false alarms are not introduced (with p = 10 used for optimization), it stands to reason that PDSL should yield greater disparity. Indeed, Figs. 9 and 10 show precisely that distinction, with the PDSL histograms for the initial and optimized cases in Fig. 9 revealing a clear and significant separation. Moreover, along with reducing PDSL, optimization also greatly reduces PDSL variance, with 98.9% of trials between −17.0 and −16.0 dB centered on the median of −16.5 dB. In contrast, this same percent of trials for initial random staggering lie between −13.5 and −8.4 dB centered on the median of −10.9 dB.

If we then determine the difference in PDSL for each intial/optimized pair of stagger sequences, Fig. 10 shows that between 3 and nearly 10 dB of improvement is obtained, with a median improvement of 5.6 dB. Per the examples in Figs. 5 and 6, we can infer that the cases with the most improvement correspond to those in which large initial sidelobe peaks occur.

Now consider the impact of the random stagger bound (also for $\beta_{opt} = 4$). As we observed in Fig. 1 from an analytical expectation perspective, increasing $\bar{\delta}$ likewise leads to a flattened Doppler response (on average). Again instantiating 1000 independent random trials, though now for distinct values of $\bar{\delta}$, we compute the ensuing mean PDSL for each $\bar{\delta}$ (prior to the log(•) calculation), with the result plotted in Fig. 11. Here we see that the difference between the initial and optimized responses is about 8 dB for $\bar{\delta} = 5\%$ and trends down to about a 6 dB difference at $\bar{\delta} = 50\%$. Of course, as noted in [26], higher $\bar{\delta}$ comes at the cost of a greater blind range swath and should therefore be avoided if possible. As Fig. 11 illustrates, there is little benefit in using $\bar{\delta} > 30\%$.

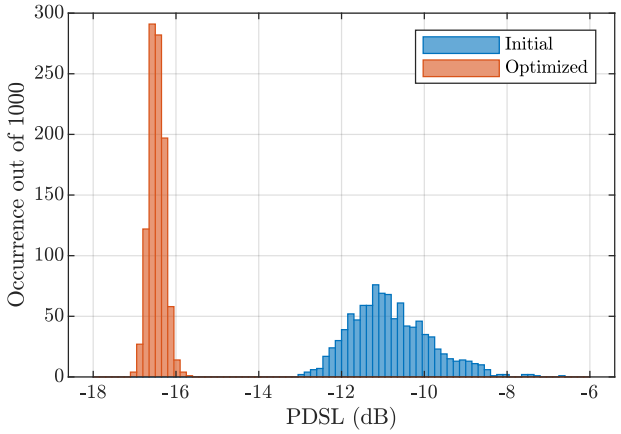

Fig. 9. Histogram of PDSL from (25) for 1000 independent initial and optimized random stagger sequences for $M = 100$, $\bar{\delta} = 30\%$, and $\beta_{opt} = 4$

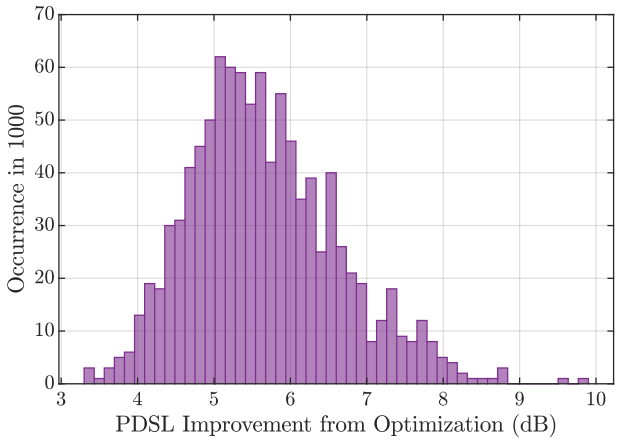

Fig. 10. Histogram of PDSL improvement between 1000 independent initial and optimized random stagger sequences for $M = 100$, $\bar{\delta} = 30\%$, and $\beta_{opt} = 4$

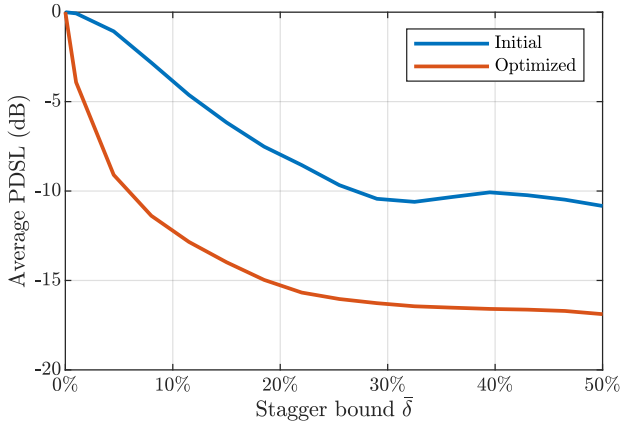

Fig. 11. Mean PDSL from (25) as a function of $\bar{\delta}$ over 1000 independent initial and optimized random stagger sequences for $M = 100$ and $\beta_{opt} = 4$

Finally, Fig. 12 illustrates an assessment similar to that in Fig. 11, albeit now with fixed $\bar{\delta} = 30\%$ and allowing the optimization Doppler span β_{opt} to vary from 1 to 20. In other words, this result represents a mean PDSL evaluation over increasing amounts of the extended Doppler interval that

increases the likelihood of a larger PDSL for initial instantiations, which the optimization then seeks to minimize.

One would intuitively expect a monotonically increasing relationship between mean PDSL and β_{opt}, which is precisely what is observed in Fig. 12. An interesting inflection exists in the vicinity of $\beta_{opt} = 2$ (noting that $f_{nD} \in [0, 0.5\beta_{opt}]$), which can be understood from the shape of the traces in Figs. 5 and 6 as the optimization span progressively expands to subsume $f_{nD} = 1$. Beyond this point the sidelobe response is considerably flatter, again due to the phase "slope deflection" discussed in [26]. For mean PDSL over the initial staggering set, less than 0.5 dB further increase is observed for $\beta_{opt} > 6$. While the optimized set incurs a slightly higher trend (about 1.5 dB as β_{opt} increases from 6 up to 20), it is also at least 3 dB lower than mean PDSL for the initial set. The gradual upward trend for both sets makes sense when considering that PDSL is being computed (or optimized) over a progressively larger span.

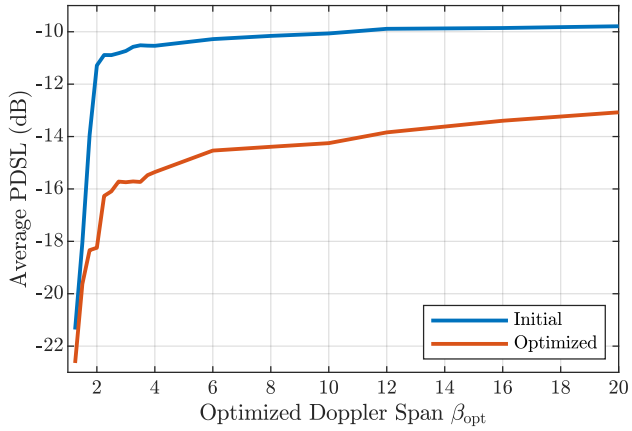

Fig. 12. Mean PDSL as a function of Doppler span β_{opt} over 1000 independent initial and optimized random stagger sequences for $M = 100$ and $\bar{\delta} = 30\%$

C. Uniqueness Assessment

A prospective benefit of random staggering from a diversity standpoint is that each CPI effectively realizes a unique sequence. While the highly nonconvex cost function of (19) suggests that the introduction of optimization should not cause a loss in uniqueness, this aspect bears further examination.

In [15], the co-array concept more commonly used for sparse array design [36] was alternatively considered in the context of PRI staggering by forming a "location" vector representing the beginning of each pulse, the autocorrelation of which yields the stagger co-array. This assessment led to the observation that some degree of co-array redundancy can actually be useful for staggering, as opposed to the *minimally redundant* attribute often sought for sparse arrays.

Here we generalize this perspective by also incorporating the pulsed waveform structure in a continuous-time context so that bandwidth (and corresponding range resolution) are also included, thereby accounting for the associated coherence span in range (see Fig. 15 in [26] and accompanying discussion). For repeated waveform $s(t)$ having unit energy, let $\tilde{s}(t)$ then denote the entire extent of the transmitted CPI, including each of the M pulsed waveforms and the zero-valued intervals in-between. Consequently, the response

$$c(\tau) = \int \tilde{s}(t)\, \tilde{s}^*(t-\tau)\, dt \tag{26}$$

captures the autocorrelation of the entire CPI [10]. For uniform PRIs, generalizing (26) to also be dependent on Doppler would yield the well-known "bed of nails" version of the delay/Doppler ambiguity function [3].

The response in (26) can also be viewed as a waveform-dependent extension of the co-array concept, an example of which is depicted in Fig. 13. We observe that the uniform case indeed produces a highly redundant triangular envelope as expected. In contrast, the random and optimized pseudo-random staggering cases exhibit far less redundancy for the simple reason that PRI intervals are no longer aligned. While the random instantiation produces an almost minimally redundant co-array, the optimized co-array does realize a modest roll-off near zero lag, indicating that a small degree of redundancy may be associated with flatter Doppler sidelobes over a fixed (and finite) interval, an attribute explored in [15].

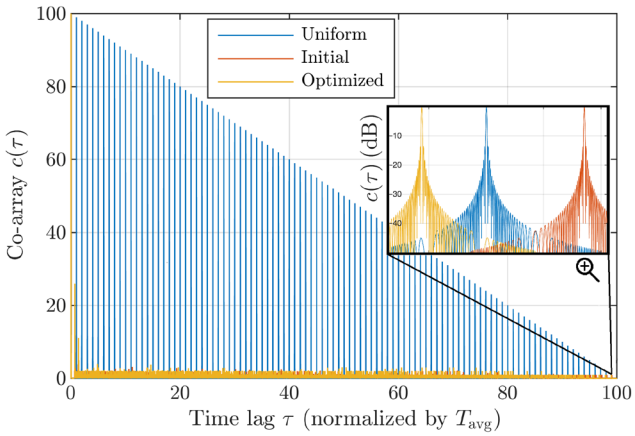

Fig. 13. Stagger co-array from (26) for $M = 100$ pulses in uniform, random, and optimized configurations shown in absolute scale demonstrating linear roll-off for uniform, and (in insert) decibel scale illustrating individual constituent waveform autocorrelations

A small modification of (26) to instead perform cross-correlation between different stagger arrangements can then be used to define a *uniqueness* metric via

$$\mu\left[\tilde{s}_1(t), \tilde{s}_2(t)\right] = \frac{1}{M} \max_{\tau} \left| \int \tilde{s}_1(t)\, \tilde{s}_2^*(t-\tau)\, dt \right|. \tag{27}$$

By using the same waveform $s(t)$ for both stagger sequences, (27) provides a normalized measure of their PRI-dependent structural similarity, the result of which lies within $[1/M, 1]$. In short, $\mu = 1$ means the sequences are identical while $\mu = 1/M$ corresponds to a single pulse correlation peak (due to unit waveform energy and normalization by M), which in turn implies no commonality between PRI intervals. A response closer to $1/M$ therefore means greater uniqueness.

Now apply this metric pairwise to 1000 independently generated sets of random stagger sequences with $M = 100$ pulses for each value of $\bar{\delta}$ between 0% and 40%, the aggregated results of which are shown in Fig. 14. We used a linear FM

(LFM) waveform with an oversampling factor (relative to swept bandwidth) of 5. Clearly the $\bar{\delta} = 0\%$ cases are comprised of uniform PRIs and are thus all identical (hence $\mu = 0$ dB). The value drops sharply as $\bar{\delta}$ increases, and beyond 10% the RMS response has essentially reached an asymptote of −15 dB, noting that $10\log_{10}(1/M) = -20$ dB for $M = 100$. The maximum and minimum value of (27) is also depicted, illustrating a fairly tight bounding about the RMS response and thereby suggesting a "typical" degree of uniqueness.

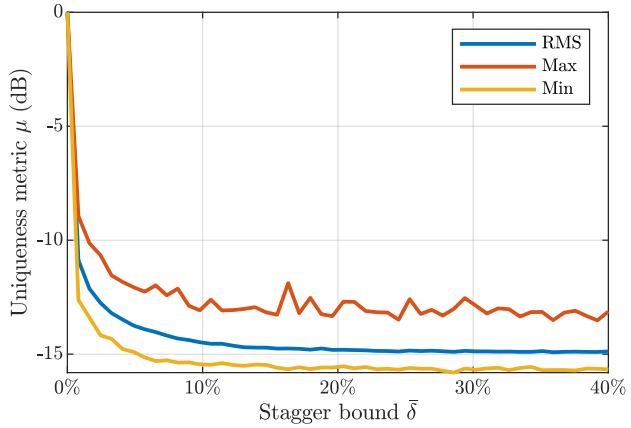

Fig. 14. Uniqueness metric from (27) applied pairwise to 1000 random stagger sequences of $M = 100$ pulses for different $\bar{\delta}$

With the behavior of purely random staggering established for the metric in (27), now consider the impact to uniqueness when optimization is performed. For $\bar{\delta}$ of 5% and 20% the 1000 independent stagger sequences used for Fig. 14 were also optimized using the gradient-descent method above (and same parameters). Each set of 1000 optimized stagger sequences was then likewise evaluated using (27) in a pairwise manner (within the given set). Figs. 15 and 16 depict the respective histograms.

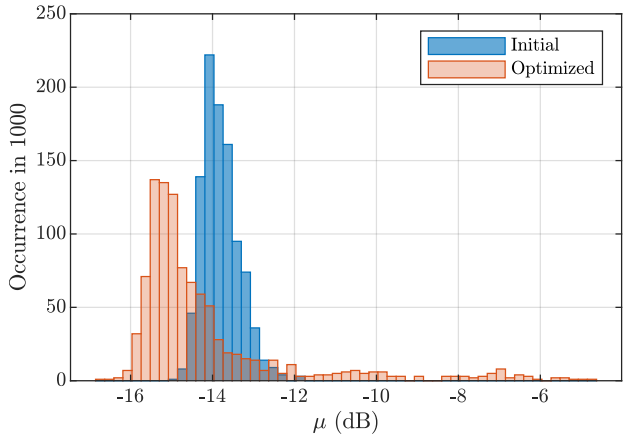

Fig. 15. Histograms for uniqueness metric from (27) applied pairwise within 1000 random stagger sequences and (separately) within 1000 optimized sequences for $M = 100$ pulses, $\beta_{opt} = 4$, and $\bar{\delta} = 5\%$

For $\bar{\delta} = 5\%$ (Fig. 15), the optimized median is −14.9 dB, compared to the initial median value of −13.9, suggesting an improvement in uniqueness overall. However, the extended tail for the optimized histogram also implies a degree of structural similarity can arise in some cases. Indeed, the largest value of μ encountered for the initial set of 1000 stagger sequences (at $\bar{\delta} = 5\%$) was −11.8 dB, while 10% of the optimized sequences exceed this value. Of course, this modest degree of allowable staggering could also be limiting the design freedom somewhat.

Now consider the $\bar{\delta} = 20\%$ case depicted in Fig. 16, where both the initial and optimized sets realize the same median of −15.0 dB. At a coarse level, the distributions are virtually identical, though optimization does again exhibit a modest tail with slightly degraded uniqueness. However, the span of uniqueness values is considerably less (and better) than that in Fig. 15, clearly indicating that greater stagger freedom translates to more consistent uniqueness between sequences.

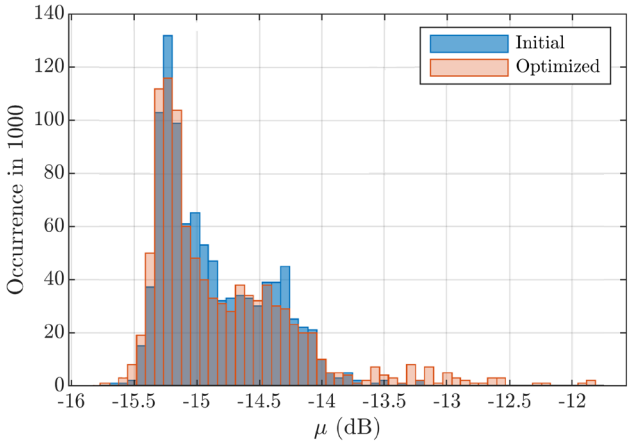

Fig. 16. Histograms for uniqueness metric from (27) applied pairwise within 1000 random stagger sequences and (separately) within 1000 optimized sequences for $M = 100$ pulses, $\beta_{opt} = 4$, and $\bar{\delta} = 20\%$

This assessment of uniqueness also leads to a related question: if the ordering of a particular sequence of staggers is shuffled, is optimized performance preserved? First consider a histogram of the metric in (27) obtained when a single arbitrary optimized sequence (using the same parameters as the set in Fig. 7) is compared to 1000 random permutations of the same set of PRIs. In so doing we find in Fig. 17 that this random shuffling actually provides a way to produce stagger sequences that are sufficiently unique from the original, even though the same PRIs are employed.

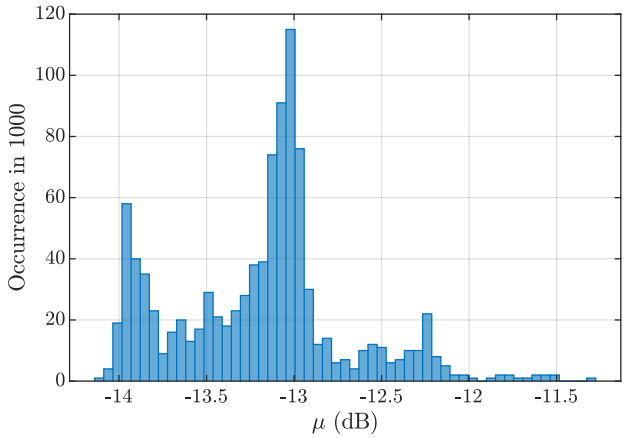

Fig. 17. Histogram for uniqueness metric from (27) applied between a single optimized stagger sequence ($M = 100$ pulses, $\beta_{opt} = 4$, and $\bar{\delta} = 30\%$) and 1000 random permutations of the same sequence

However, Fig. 18 shows that there is a price to be paid for this seemingly free generation of new stagger sequences. Here we plot the PDSL histograms from Fig. 9 along with an additional histogram obtained by randomly shuffling each optimized sequence. The extent of each CPI remains fixed because we are only permuting PRI order within each sequence and not mixing between sequences. Clearly the PDSL performance of the optimized sequences has degraded back to roughly that of the initial PDSL performance. In other words, it is not just the PRI interval values, but also their particular order, that yields the optimized flattening of extended Doppler. This result can be intuitively understood by considering that the sidelobe cancellation (flattening) effect is achieved by a phase-coherent combination via (4) and (16) determined by the accumulated PRI times from (5), which would be changed by a reordering of PRIs.

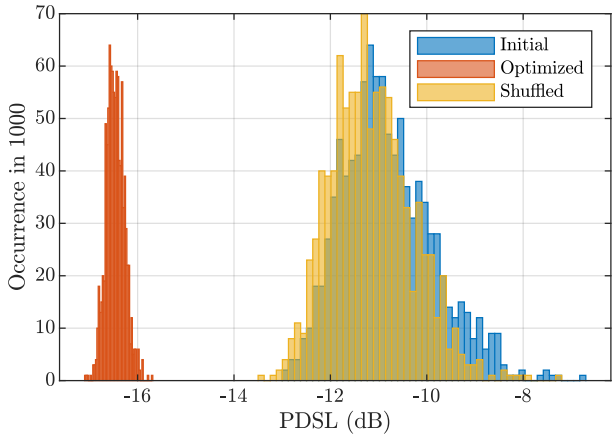

Fig. 18. Histograms of PDSL from Fig. 9 for $M = 100$, $\bar{\delta} = 30\%$, and $\beta_{\text{opt}} = 4$, with each optimized sequence having its PRIs randomly shuffled

D. Effect of CPI Scaling

As discussed in Section III-C, some PRIs may fall outside of the prescribed staggering limit when scaling is performed to preserve a fixed CPI extent. Where Fig. 4 provided a histogram of purely random PRI staggers after scaling, Fig. 19 now shows PRI histograms for 1000 trials of $M = 100$ pulse CPIs based on random initializations per (18) and the corresponding optimized sequences, using the set from Fig. 7.

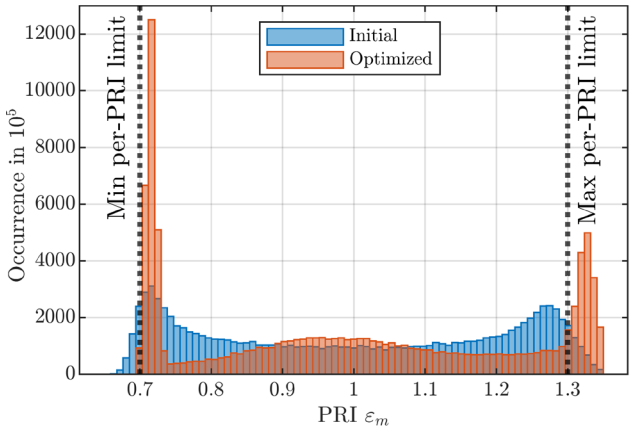

Fig. 19. Histogram of initial and optimized PRIs after scaling for 1000 trials of $M = 100$ pulses, $\bar{\delta} = 30\%$, and $\beta_{\text{opt}} = 4$

The modestly bimodal initial distribution imposed by the sine bounding function is clearly amplified by optimization, thereby worsening the impact of scaling. Relative to the near-uniform distribution (after scaling) in Fig. 4 or the sine-bounded distribution after scaling here, the scaled PRIs after optimization exhibit a notable increase in the number falling outside the design limit. However, it is interesting to observe that optimization has almost eliminated the number of extreme contraction cases (that would have exacerbated blind ranges) while growing the number of dilation cases, which is less problematic since it can be addressed by a modest increase of β_{opt} . Further, while the number of dilation cases has clearly grown, the degree has remained modest.

E. Timing Quantization

Finally, because the gradient-based optimization relies on staggering being performed on a continuum, a quick note on the impact of quantizing to a finite grid of stagger offsets, which is necessary for implementation in digital hardware. Due to the coherence span of $\pm 1/B$ (for 3-dB bandwidth B) depicted in Fig. 15 of [26], any timing quantization sufficiently less than $1/B$ experiences negligible deviation from the optimized result. With modern arbitrary waveform generators (AWGs) capable of operating at many Gigasamples/second, this effect would only need to be considered at wideband regimes. Moreover, while the receive sampling rate could conceivably be lower than what is needed for the AWG, it too must be sufficient to adequately capture spectral content.

V. Experimental Validation

Open-air measurements were collected to experimentally validate the benefit of optimized pseudo-random staggering. The intersection of 23rd and Iowa streets in Lawrence, KS was illuminated from the rooftop of Nichols Hall on the University of Kansas campus, a distance of about 1.1 km, at a center frequency of 3.45 GHz. The measurements were captured when North/South traffic accelerated after a stoplight change. The intersection contains turn lanes, so other traffic motion may be present as well. Three CPIs of 250 ms each were generated sequentially to best capture the same set of movers. Each pulse was modulated with a linear FM (LFM) chirp having a swept bandwidth of 160 MHz and a 5 μs pulsewidth (thus $TB = 800$).

To realize sufficient receive energy, the first two CPIs are composed of $M = 100$ sub-CPIs containing 10 uniformly spaced pulses at a PRF of 40 kHz. Each sub-CPI is coherently integrated via presumming after receive pulse compression, where the sub-CPIs have an effective PRF (on average) of 400 Hz, which corresponds to an unambiguous velocity interval of ±8.7 m/s for the uniform case. The random cases are based on $\bar{\delta} = 30\%$, with staggering occuring between the sub-CPIs. Consequently, the impact of Doppler aliasing/expansion can be assessed for movers within the context of a 40 mph (~17.9 m/s) speed limit and a transmit peak power of 22 dBm.

The first CPI contains an instantiation of completely random PRIs, while the second CPI is an optimized version thereof using $\beta_{\text{opt}} = 8$. Specifically, a Monte Carlo evaluation of 1000 trials using these parameters reveals a median PDSL improvement of 4.4 dB when optimizing. The particular before/

after pair depicted here realizes 6.8 dB PDSL improvement, as shown in Fig. 20 referenced to a hypothetical mover at the outermost positive edge of the radial velocity span.

The third and final CPI contains 200 sub-CPIs having a uniform arrangement and an effective PRF of 800 Hz. Consequently, this case serves as a ground truth in which no Doppler aliasing occurs. Moreover, to establish an arrangement of 100 sub-CPIs at an effective PRF of 400 Hz that is commensurate with the staggering cases, we need only down-select to use every-other uniform sub-CPI.

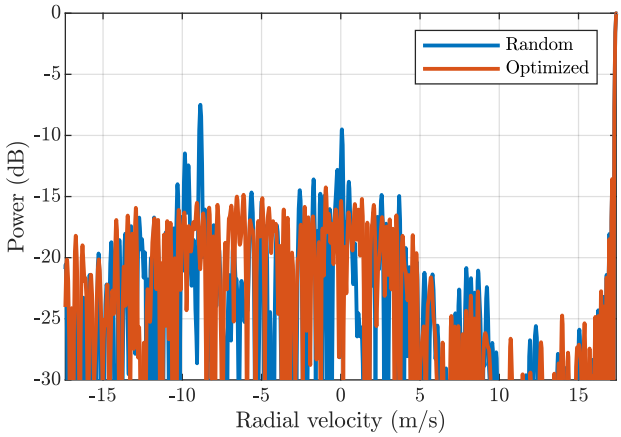

Fig. 20. Instantiation of random staggering and optimized pseudo-random staggering for $M = 100$, $\bar{\delta} = 30\%$ and $\beta_{\text{opt}} = 8$ used in subsequent open-air measurements. Response is referenced to a hypothetical mover at the speed limit. (6.8 dB PDSL improvement)

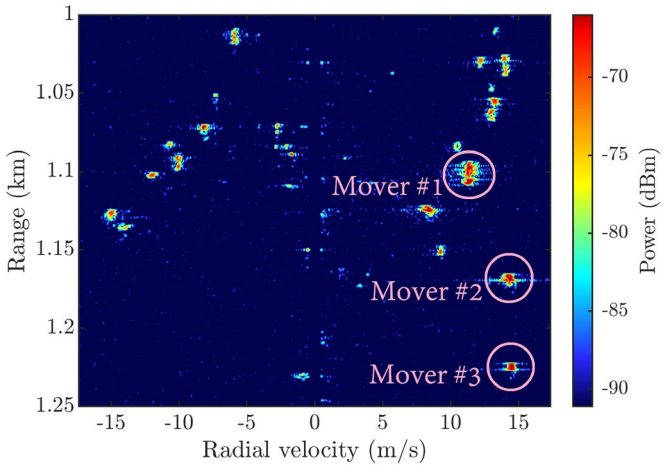

Fig. 21. Ground truth range-Doppler response for uniform sub-CPIs without Doppler aliasing (effective PRF = 800 Hz)

Each CPI is pulse compressed using a Hamming-weighted mismatched filter to reduce range sidelobes so the ensuing analysis can focus on Doppler sidelobe behavior. The resulting range-Doppler responses after pulse compression, presumming the 10 pulses in each sub-CPI, clutter cancellation (projection at/around zero Doppler), and Doppler processing are shown in Figs. 21-24. Fig. 21 illustrates the ground truth uniform sub-CPI case in which the effective PRF (800 Hz) is high enough to prevent Doppler aliasing. Moreover, three particular movers have been identified for comparison in the results that follow. Indeed, Fig. 22 depicts the down-selected uniform case having an effective PRF of 400 Hz, where we observe that these three movers (and all the rest) are clearly aliased.

Now consider the impact of staggering shown in Figs. 23 and 24 for completely random and optimized pseudo-random, respectively. We see that the unambiguous Doppler space has been expanded so that aliasing is now avoided, though the cost of doing so is a Doppler sidelobe response containing spurious sidelobes in the form of false peaks (compared to Fig. 21) and horizontal streaks across Doppler. The optimized case in Fig. 24 manages to avoid the false peaks, yet a cursory evaluation would seem to indicate that the streaks across Doppler are actually worse. Consequently, a closer examination is needed.

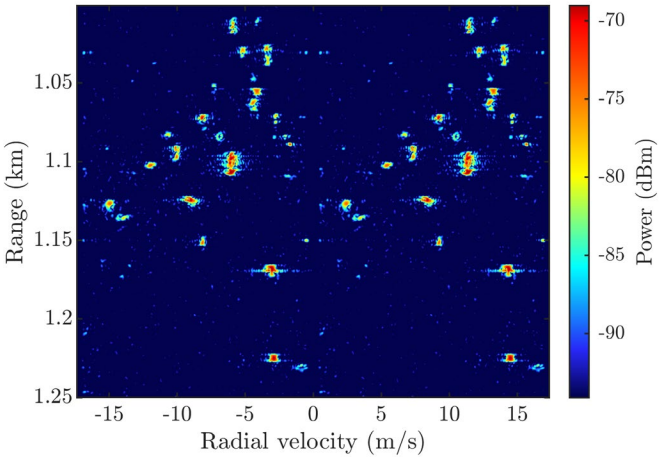

Fig. 22. Range-Doppler response for down-selected uniform sub-CPIs causing Doppler aliasing to occur (effective PRF = 400 Hz)

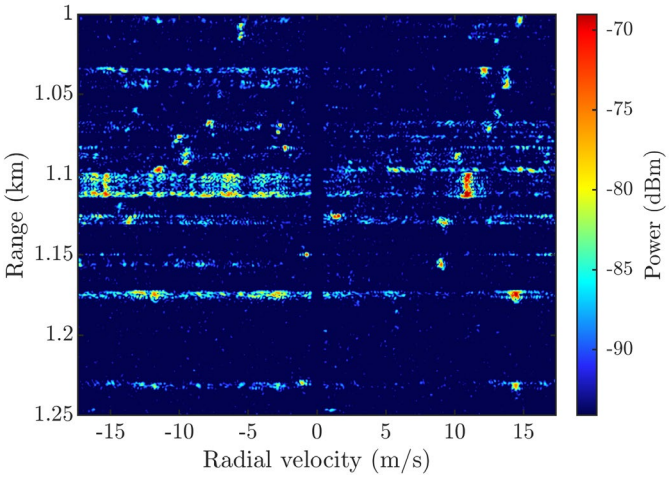

Fig. 23. Range-Doppler response for random sub-CPIs (average effective PRF = 400 Hz). Aliasing is avoided at the cost of higher Doppler sidelobes.

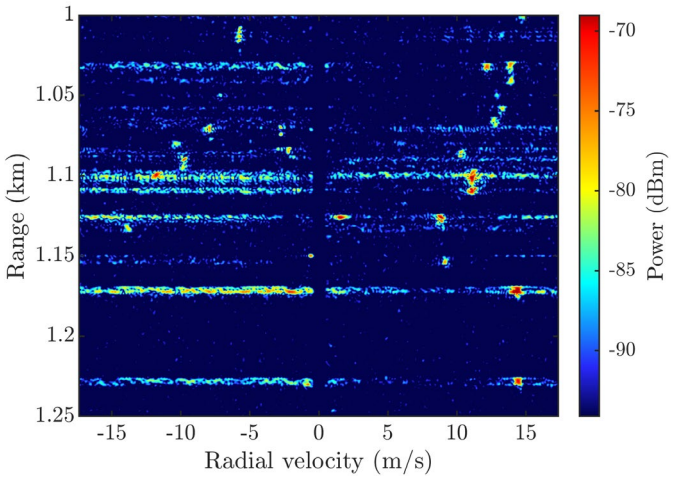

Fig. 24. Range-Doppler response for optimized pseudo-random sub-CPIs (average effective PRF = 400 Hz). Aliasing is avoided and Doppler sidelobes are flattened to the degree possible.

Figs. 25 and 26 provide Doppler slices at the particular range cells corresponding to Movers #2 and #3, respectively, in which a 3 dB and 5 dB scintillation effect is observed. This variation in received SNR from one CPI to the next likewise translates into a variation in sidelobe level, though the Doppler sidelobes are also different due to random or optimized structures. Thus, when optimization is performed Mover #2 collectively experiences 10.5 – 5.6 = 4.9 dB improvement in PDSL, while Mover #3 has 10.7 – 6.8 = 3.9 dB improvement.

Figs. 27 and 28 also provide close-up range-Doppler views of the sidelobes induced by Mover #1, which exhibits some extent in range and is likely a large truck (typical length is ~22 meters). The dynamic range depicted is also reduced somewhat to enhance visibility. In Fig. 27 we observe two pairs of false peaks that are separated by roughly 8-10 m/s in Doppler, coinciding with the spurious Doppler sidelobes observed in Fig. 20 for this stagger instantiation. In contrast, Fig. 28 reveals a flattened sidelobe response that permits a different mover (identified in Fig. 27) to remain visible despite it now falling within those very sidelobes.

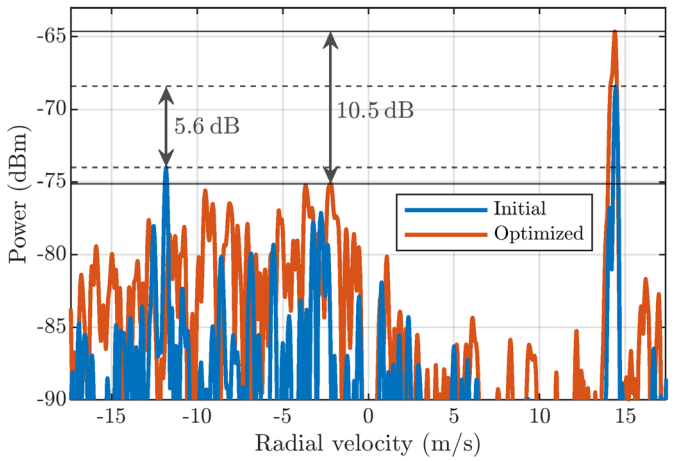

Fig. 25. Doppler slice for Mover #2 range cell showing optimization yields a PDSL improvement of 4.9 dB

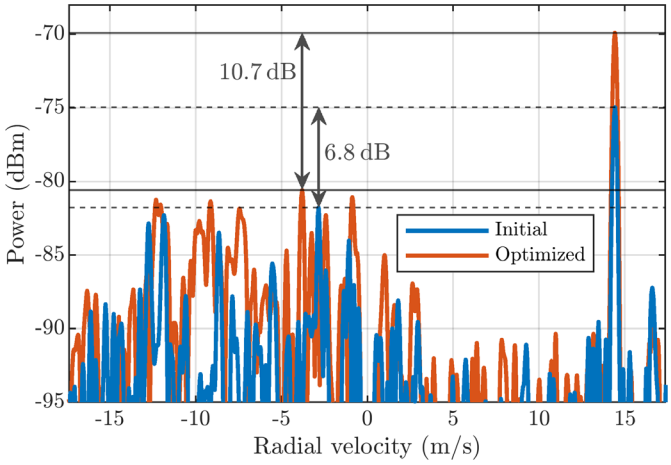

Fig. 26. Doppler slice for Mover #3 range cell showing optimization yields a PDSL improvement of 3.9 dB

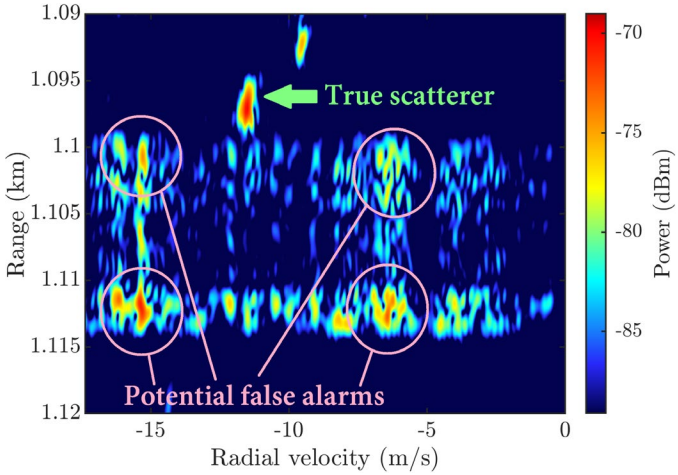

Fig. 27. Close-up range-Doppler response of sidelobes induced by (range-extended) Mover #1 for completely random staggering

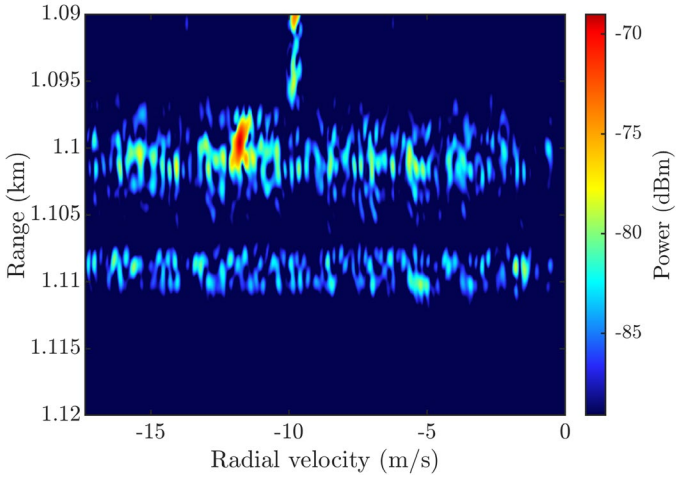

Fig. 28. Close-up range-Doppler response of sidelobes induced by (range-extended) Mover #1 for optimized pseudo-random staggering

Finally, it bears repeating that only $M = 100$ sub-CPIs were used for these open-air measurements, meaning the optimization-flattened sidelobe pedestal could at best approach $-10 \log_{10}(M) = -20$ dB, with a few dB less actually observed from the various Monte Carlo analyses. Thus, the improvement

achieved by optimization is expected to be greater for higher M, especially relative to worst-case random instantiations.

VI. Conclusions

It is well-known that random PRI staggering provides the means to expand the unambiguous Doppler space. However, it does so at the potential cost of high spurious sidelobes. Here a p-norm based approach has been developed, analyzed, and experimentally demonstrated in the Doppler context to provide a way to achieve pseudo-random staggering sequences via a gradient-descent optimization. The highly non-convex nature of the cost function also essentially ensures that uniqueness imposed by randomness is preserved. While beyond the scope of the present paper, it is expected that combining such optimized staggering with adaptive receive processing (e.g. such as recently experimentally demonstrated in [37] for purely random staggering) could be a useful pairing.

Appendix A

The following details the derivation of the gradient depicted in (20) and (21). First, rewrite (16) as

$$\begin{aligned}\mathbf{u}(\boldsymbol{\varepsilon}) &= \frac{1}{M}\mathbf{V}^H\mathbf{v}_0 \\ &= \frac{1}{M}(\mathbf{v}_0^T\otimes\mathbf{I}_{N\times N})\,\mathrm{vec}\{\mathbf{V}^H\} \\ &= \frac{1}{M}(\mathbf{v}_0^T\otimes\mathbf{I}_{N\times N})\,\overline{\mathbf{v}}_{NM\times 1}\end{aligned} \tag{28}$$

where $\mathrm{vec}\{\bullet\}$ is the *vectorization* operation [39], $\otimes$ is the Kronecker product, and $\mathbf{I}$ is an identity matrix. Both the second line of (28) and the third-line replacement with

$$\begin{aligned}\overline{\mathbf{v}}_{NM\times 1} &= \mathrm{vec}\{\mathbf{V}^H\} \\ &= \exp\left\{-j2\pi\,\mathrm{vec}\{\mathbf{f}_{\mathrm{nD}}\,\boldsymbol{\varepsilon}^T\mathbf{B}^T\}\right\} \\ &= \exp\left\{-j2\pi\,(\mathbf{B}\otimes\mathbf{f}_{\mathrm{nD}})\,\boldsymbol{\varepsilon}\right\}\end{aligned} \tag{29}$$

rely on the identity $\mathrm{vec}\{\mathbf{XYZ}\} = (\mathbf{Z}^T\otimes\mathbf{X})\mathrm{vec}\{\mathbf{Y}\}$, with $\exp\{\bullet\}$ denoting element-wise exponentiation. For convenience, let

$$\boldsymbol{\theta}_{NM\times 1} = (\mathbf{B}\otimes\mathbf{f}_{\mathrm{nD}})\,\boldsymbol{\varepsilon} \tag{30}$$

so that (29) becomes

$$\overline{\mathbf{v}}_{NM\times 1} = \exp\left\{-j2\pi\,\boldsymbol{\theta}_{NM\times 1}\right\}. \tag{31}$$

Suppressing the explicit dependence on $\boldsymbol{\alpha}$ for compactness, rewrite (19) as

$$J_p = \frac{\left\|\mathbf{w}_{\mathrm{sl}}\odot\mathbf{u}\right\|_p^2}{\left\|\mathbf{w}_{\mathrm{ml}}\odot\mathbf{u}\right\|_p^2} = \left(\frac{\mathbf{w}_{\mathrm{sl}}^T|\mathbf{u}|^p}{\mathbf{w}_{\mathrm{ml}}^T|\mathbf{u}|^p}\right)^{(2/p)}. \tag{32}$$

By the chain rule and leveraging aspects of [27], the partial derivative of (19) with respect to α_m is then

$$\begin{aligned}\frac{\partial J_p}{\partial\alpha_m} = &\left(\frac{2}{p}\right)J_p\times \\ &\left[\frac{1}{\mathbf{w}_{\mathrm{sl}}^T|\mathbf{u}|^p}\left(\mathbf{w}_{\mathrm{sl}}^T\frac{\partial|\mathbf{u}|^p}{\partial\alpha_m}\right)-\frac{1}{\mathbf{w}_{\mathrm{ml}}^T|\mathbf{u}|^p}\left(\mathbf{w}_{\mathrm{ml}}^T\frac{\partial|\mathbf{u}|^p}{\partial\alpha_m}\right)\right]\end{aligned} \tag{33}$$

in which

$$\begin{aligned}\frac{\partial|\mathbf{u}|^p}{\partial\alpha_m} &= p|\mathbf{u}|^{(p-2)}\odot\left[\left(\frac{\partial}{\partial\alpha_m}\mathbf{u}\right)\odot\mathbf{u}^*+\mathbf{u}\odot\left(\frac{\partial}{\partial\alpha_m}\mathbf{u}^*\right)\right] \\ &= p|\mathbf{u}|^{(p-2)}\odot\Re\left\{\left(\frac{\partial}{\partial\alpha_m}\mathbf{u}\right)\odot\mathbf{u}^*\right\}\end{aligned} \tag{34}$$

for $\Re\{\bullet\}$ the real part of the argument. Using (28)-(31) and following the chain rule, the partial derivative in (34) subsequently becomes

$$\begin{aligned}\frac{\partial}{\partial\alpha_m}\mathbf{u} &= \frac{1}{M}\frac{\partial}{\partial\alpha_m}\left[(\mathbf{v}_0^T\otimes\mathbf{I}_{N\times N})\,\overline{\mathbf{v}}\right] \\ &= \frac{1}{M}(\mathbf{v}_0^T\otimes\mathbf{I}_{N\times N})\;\frac{\partial}{\partial\alpha_m}\left[\overline{\mathbf{v}}\right] \\ &= \frac{1}{M}(\mathbf{v}_0^T\otimes\mathbf{I}_{N\times N})\frac{\partial}{\partial\alpha_m}\left[\exp\{-j2\pi\,\boldsymbol{\theta}\}\right] \\ &= \frac{-j2\pi}{M}(\mathbf{v}_0^T\otimes\mathbf{I}_{N\times N})\left[\exp\{-j2\pi\,\boldsymbol{\theta}\}\odot\frac{\partial}{\partial\alpha_m}[\boldsymbol{\theta}]\right] \\ &= \frac{-j2\pi}{M}(\mathbf{v}_0^T\otimes\mathbf{I}_{N\times N})\left[\overline{\mathbf{v}}\odot\frac{\partial}{\partial\alpha_m}\left[(\mathbf{B}\otimes\mathbf{f}_{\mathrm{nD}})\,\boldsymbol{\varepsilon}\right]\right] \\ &= \frac{-j2\pi}{M}(\mathbf{v}_0^T\otimes\mathbf{I}_{N\times N})\left[\overline{\mathbf{v}}\odot\left[(\mathbf{B}\otimes\mathbf{f}_{\mathrm{nD}})\;\frac{\partial}{\partial\alpha_m}[\boldsymbol{\varepsilon}]\right]\right] \\ &= \frac{+j2\pi\bar{\delta}}{M}(\mathbf{v}_0^T\otimes\mathbf{I}_{N\times N})\left[\overline{\mathbf{v}}\odot\left[(\mathbf{B}\otimes\mathbf{f}_{\mathrm{nD}})(\cos\{\boldsymbol{\alpha}\}\odot\mathbf{e}_m)\right]\right],\end{aligned} \tag{35}$$

where $\mathbf{e}_m$ is an $M\times 1$ elementary vector in which the mth element is 1 and the rest are zero.

Using the identity following (29) to now sequentially undo the vectorization operation leads to (35) becoming

$$\begin{aligned}\frac{\partial}{\partial\alpha_m}\mathbf{u} &= \frac{+j2\pi\bar{\delta}}{M}(\mathbf{v}_0^T\otimes\mathbf{I}_{N\times N})\left[\overline{\mathbf{v}}\odot\left[(\mathbf{B}\otimes\mathbf{f}_{\mathrm{nD}})(\cos\{\boldsymbol{\alpha}\}\odot\mathbf{e}_m)\right]\right] \\ &= \frac{+j2\pi\bar{\delta}}{M}(\mathbf{v}_0^T\otimes\mathbf{I}_{N\times N})\left[\overline{\mathbf{v}}\odot\mathrm{vec}\left\{\mathbf{f}_{\mathrm{nD}}(\cos\{\boldsymbol{\alpha}\}\odot\mathbf{e}_m)^T\mathbf{B}^T\right\}\right] \\ &= \frac{+j2\pi\bar{\delta}}{M}(\mathbf{v}_0^T\otimes\mathbf{I}_{N\times N}) \\ &\qquad\times\left[\mathrm{vec}\left\{\mathbf{V}^H\odot\left(\mathbf{f}_{\mathrm{nD}}(\cos\{\boldsymbol{\alpha}\}\odot\mathbf{e}_m)^T\mathbf{B}^T\right)\right\}\right] \\ &= \frac{+j2\pi\bar{\delta}}{M}\left(\mathbf{V}^H\odot\left(\mathbf{f}_{\mathrm{nD}}(\cos\{\boldsymbol{\alpha}\}\odot\mathbf{e}_m)^T\mathbf{B}^T\right)\right)\mathbf{v}_0,\end{aligned}$$

(36)

which is convenient from a computational perspective by avoiding the need to perform Kronecker products. Substituting (36) back into (34) yields

$$\begin{aligned}\frac{\partial|\mathbf{u}|^p}{\partial\alpha_m} &= p|\mathbf{u}|^{(p-2)} \odot \Re\left\{\left(\frac{\partial}{\partial\alpha_m}\mathbf{u}\right)\odot\mathbf{u}^*\right\} \\ &= \frac{2\pi\bar{\delta}}{M}\, p\left[|\mathbf{u}|^{(p-2)} \odot \Im\left\{\left(\left(\mathbf{V}^H \odot \left(\mathbf{f}_{\mathrm{nD}}(\cos\{\boldsymbol{\alpha}\}\odot\mathbf{e}_m)^T\mathbf{B}^T\right)\right)\mathbf{v}_0\right)\odot\mathbf{u}^*\right\}\right] \\ &= \frac{2\pi\bar{\delta}}{M}\, p\,\mathbf{g}_m\end{aligned} \tag{37}$$

where we have denoted $\mathbf{g}_m$ as the vector inside the brackets [•] comprising the Hadamard product between $\mathbf{u}^{(p-2)}$ and the $\Im\{\bullet\}$ component, which takes the imaginary part of the argument. Then substituting (37) into (33) produces

$$\begin{aligned}\frac{\partial J_p}{\partial\alpha_m} &= \frac{4\pi\bar{\delta}}{M} J_p\left[\frac{\mathbf{w}_{\mathrm{sl}}^T}{\mathbf{w}_{\mathrm{sl}}^T|\mathbf{u}|^p} - \frac{\mathbf{w}_{\mathrm{ml}}^T}{\mathbf{w}_{\mathrm{ml}}^T|\mathbf{u}|^p}\right]\mathbf{g}_m \\ &= \frac{4\pi\bar{\delta}}{M} J_p\,\mathbf{g}_m^T\left[\frac{\mathbf{w}_{\mathrm{sl}}}{\mathbf{w}_{\mathrm{sl}}^T|\mathbf{u}|^p} - \frac{\mathbf{w}_{\mathrm{ml}}}{\mathbf{w}_{\mathrm{ml}}^T|\mathbf{u}|^p}\right],\end{aligned} \tag{38}$$

where the bottom form of (38) permits collection of the $m = 1, 2, \ldots, M-1$ terms (recalling that $\varepsilon_0 = \alpha_0 = 0$) as

$$\nabla_{\boldsymbol{\alpha}} J_p = \frac{4\pi\bar{\delta}}{M} J_p\,\mathbf{G}^T\left[\frac{\mathbf{w}_{\mathrm{sl}}}{\mathbf{w}_{\mathrm{sl}}^T|\mathbf{u}|^p} - \frac{\mathbf{w}_{\mathrm{ml}}}{\mathbf{w}_{\mathrm{ml}}^T|\mathbf{u}|^p}\right] \tag{39}$$

for $N \times M$ matrix

$$\mathbf{G} = \left[\mathbf{0}_{N\times 1}\ \ \mathbf{g}_1 \cdots \mathbf{g}_{M-1}\right]. \tag{40}$$

As an aside, one could consider other bounding functions besides the $\sin(\alpha_m)$ approach in (18) as long as the function is continuous and its output maps to the interval [–1, +1]. For instance, the hyperbolic tangent function $\tanh(\alpha_m)$ could alternatively be used, with the previously resulting $\cos(\alpha_m)$ term in (35) then being replaced by $\mathrm{sech}^2(\alpha_m)$.

REFERENCES

[1] M.A. Richards, J.A. Scheer, W.A. Holm, eds., *Principles of Modern Radar: Basic Principles*. SciTech Publishing, Raleigh, NC, 2010.

[2] D.C. Schleher, *MTI and Pulsed Doppler Radar*. Artech House, Boston, MA, 2008.

[3] N. Levanon, E. Mozeson, *Radar Signals*. John Wiley Sons, Inc., Hoboken, NJ, 2004.

[4] S.A. Hovanessian, "An algorithm for calculation of range in a multiple PRF radar," *IEEE Trans. Aerospace & Electronic Systems*, vol. 12, no. 2, pp. 287-290, Mar. 1976.

[5] G.V. Trunk, S. Brockett, "Range and velocity ambiguity resolution," *IEEE National Radar Conf.*, Lynnfield, MA, Apr. 1993.

[6] G.V. Trunk, M.W. Kim, "Ambiguity resolution of multiple targets using pulse-Doppler waveforms," *IEEE Trans Aerospace & Electronic Systems*, vol. 30, no. 4, pp. 1130-1137, Oct. 1994.

[7] M. Skolnik, *Radar Handbook*, 3rd ed., McGraw-Hill, New York, NY, 2008.

[8] P. Stinco, M. Greco, F. Gini, A. Farina, L. Timmoneri, "Analysis and comparison of two disambiguity algorithms: The modified CA and CRT," *Intl. Radar Conf.,* Bordeaux, France, Oct. 2009.

[9] F.D. Almeida García, *et al*., "Probability of detection for unambiguous Doppler frequencies in pulsed radars using the Chinese remainder theorem and subpulse processing," *53rd Asilomar Conf. Signals, Systems, & Computers*, Pacific Grove, CA, Nov. 2019.

[10] A.W. Rihaczek, "Radar resolution properties of pulse trains," *Proc. IEEE*, vol. 52, no. 2, pp. 153-164, Feb. 1964.

[11] R. Roy, O. Lowenschuss, "Design of MTI detection filters with nonuniform interpulse periods," *IEEE Trans. Circuit Theory*, vol. 17, no. 4, pp. 604-612, Nov. 1970.

[12] M.A. Arbabian, M.H. Bastani, M. Tabesh, "Optimization of PRF staggering in MTI radar," *IEEE Radar Conf.*, Arlington, VA, May 2005.

[13] M. Villano, G. Krieger, A. Moreira, "Staggered-SAR for high-resolution wide-swath imaging," *IET Intl. Conf. Radar Systems,* Glasgow, UK, Oct. 2012.

[14] M. Villano, G. Krieger, A. Moreira, "Staggered SAR: high-resolution wide-swath imaging by continuous PRI variation," *IEEE Trans. on Geoscience & Remote Sensing*, vol. 52, no. 7, pp. 4462-4479, July 2014.

[15] R.J. Chang, D.B. Herr, J.W. Owen, P.M. McCormick, S.D. Blunt, J.M. Stiles, "On the relationship between PRI staggering and sparse arrays," *IEEE Radar Conf.*, San Antonio, TX, May 2023.

[16] J.K. Hsiao, "On the optimization of MTI clutter rejection," *IEEE Trans. Aerospace & Electronic Systems*, vol. 10, no. 5, pp. 622-629, Sept. 1974.

[17] M. Kaveh, G.R. Cooper, "Average ambiguity function for a randomly staggered pulse sequence," *IEEE Trans. Aerospace & Electronic Systems*, vol. 12, no. 3, pp. 410–413, May 1976.

[18] L.B. Milstein, "Reduction of eclipsing loss in high PRF radars," *IEEE Trans. Aerospace & Electronic Systems,* vol. 14, no. 2, pp. 410-415, Mar. 1978.

[19] R. Benjamin, "Form of Doppler processing for radars of random p.r.i. and r.f. ," *Electronics Letters*, vol. 15, no. 24, pp. 782, Feb. 1979.

[20] L. Vergara-Dominguez, "Analysis of the digital MTI filter with random PRI," *IEE Proc. F - Radar & Signal Processing,* vol. 140, no. 2, pp. 129-137, Apr. 1993.

[21] M. Modarres-Hashemi, M.M. Nayebi, "Performance evaluation of random PRF signals in LPD radars," *IEEE Intl. Radar Conf.,* Alexandria, VA, pp. 134-139, May 2000.

[22] Z. Liu, X. Wei, X. Li, "Aliasing-free moving target detection in random pulse repetition interval radar based on compressive sensing," *IEEE Sensors Journal*, vol. 13, no. 7., pp. 2523-2534, July 2013.

[23] J. Zhu, T. Zhao, T. Huang, D. Zhang, "Analysis of random pulse repetition interval radar," *IEEE Radar Conf.*, Philadelphia, PA, May 2016.

[24] W.L. van Rossum, L. Anitori, "Simultaneous resolution of range-Doppler ambiguities using agile pulse intervals with sparse signal processing," *IEEE Radar Conf.,* Florence, Italy, Sept. 2020.

[25] X. Long, K. Li, J. Tian, J. Wang, S. Wu., "Ambiguity function analysis of random frequency and PRI agile signals," *IEEE Trans. Aerospace & Electronic System*s, vol. 57, no. 1, pp. 382-396, Feb. 2021.

[26] S.D. Blunt, L.A. Harnett, B. Ravenscroft, R.J. Chang, C.T. Allen, P.M. McCormick, "Implications of diversified Doppler for random PRI radar," to appear in *IEEE Trans. Aerospace & Electronic Systems.*

[27] C.A. Mohr, P.M. McCormick, C.A. Topliff, S.D. Blunt, J.M. Baden, "Gradient-based optimization of PCFM radar waveforms," *IEEE Trans. Aerospace & Electronic Systems*, vol. 57, no. 2, pp. 935-956, Apr. 2021.

[28] P.J.A. Prinsen, "Elimination of blind velocities of MTI radar by modulating the interpulse period," *IEEE Trans. Aerospace & Electronic Systems*, vol. 9, no. 5, pp. 714-724, Sept. 1973.

[29] L. de Martín, W. van Rossum, "Optimization of pulse intervals for unambiguous Doppler recovery with oversampled dictionary," *IEEE Radar Conf.,* New York City, NY, Mar. 2022.

[30] J.M. Baden, M.S. Davis, L. Schmeider, "Energy efficient gradient calculations for binary and polyphase sequences," *IEEE Intl. Radar Conf*., Washington, DC, May 2015.

[31] S.D. Blunt, M. Cook, J. Jakabosky, J. de Graaf, E. Perrins, "Polyphase-coded FM (PCFM) radar waveforms, part I: implementation," *IEEE*

Trans. Aerospace & Electronic Systems, vol. 50, no. 3, pp. 2218-2229, July 2014.

[32] P.S. Tan, J. Jakabosky, J.M. Stiles, S.D. Blunt, "Higher-order implementations of polyphase-coded FM radar waveforms," *IEEE Trans. Aerospace & Electronic Systems*, vol. 55, no. 6, pp. 2850-2870, Dec. 2019.

[33] B. White, M.B. Heintzelman, S.D. Blunt, "Alternative 'bases' for gradient-based optimization of parameterized FM radar waveforms," *IEEE Radar Conf*., San Antonio, TX, May 2023.

[34] D.C. Liu, J. Nocedal, "On the limited memory BFGS method for large scale optimization," *Mathematical Programming,* vol. 45, pp. 503–528, Aug. 1989.

[35] N. Vervliet, O. Debals, L. Sorber, M. Van Barel, L. De Lathauwer, *Tensorlab 3.0*, https://www.tensorlab.net/, Mar. 2016.

[36] A. Moffet, "Minimum-redundancy linear arrays," *IEEE Trans. Antennas & Propagation*, vol. 16, no. 2, pp. 172-175, Mar. 1968.

[37] L.A. Harnett, B. Ravenscroft, S.D. Blunt, C.T. Allen, "Experimental evaluation of adaptive Doppler estimation for PRI-staggered radar," *IEEE Radar Conf*., New York City, NY, Mar. 2022.

[38] K.B. Petersen, M.S. Pedersen, *The Matrix Cookbook,* Nov. 2012.